23

X-ray dark field imaging

© V.V. Lider

National Research Center „Kurchatov Institute“,
123182 Moscow, Russia

e-mail: vallider@yandex.ru

Received September 09, 2023
Revised February 16, 2024
Accepted March 27, 2024

X-ray imaging in a dark field has found application in recent years in various fields of science and technology, including medicine, biology, and materials science. The review is devoted to the description of various methods of X-ray dark-field visualization. Experimental optical schemes of the methods, methods of data collection and processing, prospects and limitations of their use are considered. Particular attention is paid to multimodal methods capable of separating the small-angle scattering signal from the absorption and phase-contrast signals.

Keywords: x-rays, visualization, dark field, multimodal methods, Talbot interferometer, crystal analyzer, x-ray grating, x-ray grid.

DOI: 10.61011/EOS.2024.04.58889.127-24

1. Introduction

In a broad sense, dark-field imaging is the study of objects with the use of radiation that the objects themselves direct to a detector; in contrast to bright-field imaging, no radiation from any external sources is detected directly in this case. In other words, unscattered photons do not produce a contribution to images of any form [1].

Common X-ray images are obtained under direct illumination (i.e., based on absorption bright-field contrast). However, absorption contrast is often insufficient to resolve fine details of samples associated with small density changes or local deformations. Dark-field imaging techniques then come to the aid of a researcher. These methods have found application in medicine [2], in the study of composite materials [3] and mineral building materials [4], and in luggage screening at airports [5].

Measurement methods may be divided tentatively into direct and indirect ones. By direct methods we mean measurements in which the sought-for parameter value is determined directly from experimental data. Indirect measurements are those in which the numerical value of the quantity to be measured is determined using a known functional dependence involving other quantities that may be evaluated by direct measurements.

X-ray microscopy [6,7] and the Laue analyzer method [8] should be classified as direct X-ray dark-field imaging methods. Indirect dark-field methods include multimodal X-ray imaging techniques, such as the propagation-based method [9], Talbot interferometer [10], the edge illumination method [11], the Bragg analyzer method [12], the speckle-based method [13], and the single-grid method [14].

The purpose of the present review is to familiarize the reader with the operating principles, specific features, and capabilities of both direct and indirect methods of X-ray dark-field imaging.

2. Direct dark-field imaging methods

Let us assume that thin („pencil“) monochromatic X-ray beam A (Fig. 1, *a*) illuminates statistically homogeneous plate B with a spatially unresolved subpixel microstructure. As a result of passing through plate B, the unresolved microstructure will expand the beam into fan C with

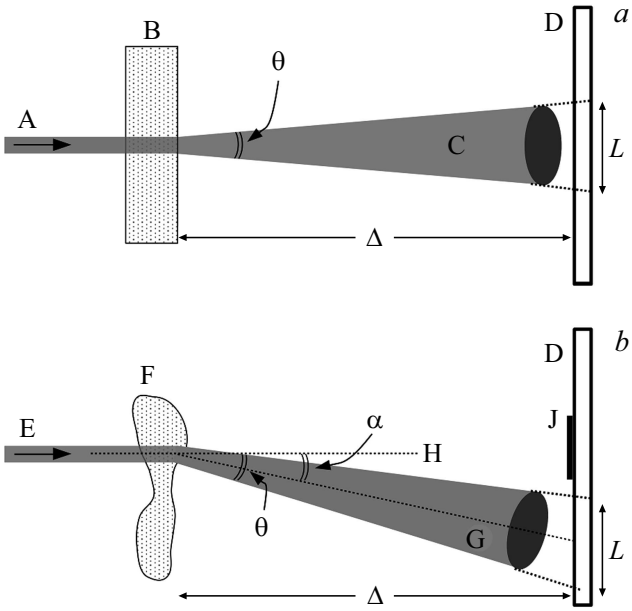

Figure 1. Illustration of changes in the shape and direction of pencil monochromatic X-ray beam A(E) incident onto statistically homogeneous plate B with a spatially unresolved microstructure (sample F containing a spatially inhomogeneous macrostructure). The transmitted beam expands into SAXS fan C(G). D — detector, J — blanking element for the direct beam, Δ — sample–detector distance, L — image blurring, θ — C(G) cone angle, and α — refraction angle [15].

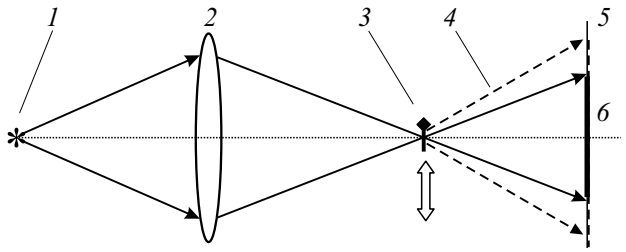

Figure 2. Optical circuit of an STXM: *1* — point X-ray source (focus formed by a condenser), *2* — objective lens, *3* — sample under study, *4* — scattered radiation, *5* — detector, and *6* — blank for blocking unscattered radiation.

cone angle θ. This expansion is associated with small-angle X-ray scattering (SAXS) that occurs when transmitted X-rays undergo multiple refraction/scattering by random structures in a sample. „SAXS fan" expansion angle θ and distance Δ between plate B and detector D specify image blurring L [15]:

$$L(x, y) = \theta(x, y)\Delta. \quad (1)$$

Since plate B is statistically homogeneous, the SAXS fan expansion angle does not depend on transverse position (x, y) of the X-ray beam illuminating the plate.

If a sample has a spatially unresolved random microstructure with its statistical properties varying with position within the sample, it is also natural to assume that the sample exhibits macrostructural changes that are modeled by X-ray refraction (phase shift) and vary with transverse beam position (x, y). Under the influence of structural inhomogeneities of sample F, incident monochromatic X-ray beam E is in this case (Fig. 1, *b*) refracted at angle α to optical axis H and is scattered into fan G [15].

For the detector to record the dark-field signal only, one just needs to place blank J in front of it in the direct beam trajectory. This principle is utilized in the design of X-ray scanning microscopes.

2.1. X-ray microscopy method

X-ray microscopy allows one to obtain an image of the object being studied in real space with the use of focusing optics elements [7,16]. Two main types of transmission X-ray microscopes are known: scanning transmission X-ray microscopes (STXMs) and conventional transmission X-ray microscopes (TXMs), which are often referred to as full-field X-ray microscopes. In an STXM (Fig. 2), an objective lens focuses an X-ray beam into a small spot on a sample, the sample is raster scanned, and the output intensity at each scanning position is recorded by a detector. Most STXMs use detectors without spatial resolution that integrate radiation transmitted through the sample.

A combination of a detector and a blank may be replaced by a segmented detector [17,18]. Figure 3, *a* presents the external view of a detector with seven segments. Segments *1–3* record the cone of light coming from the studied object and produce bright-field contrast [18]. Segments *4–7* may be used to obtain dark-field images. Figure 3, *b* demonstrates the superiority of dark-field imaging (an image is formed by the difference in X-ray intensities recorded by segments *4, 5* and *6, 7*) over bright-field contrast (all segments are illuminated by X-rays) [17].

The optical circuit of a TXM (Fig. 4) is very similar to the one of a conventional light microscope. A TXM features a condenser (not shown) and an objective lens. The latter produces an enlarged image of a sample in the detection plane that is recorded by a pixel detector (a charge-coupled device (CCD) is normally used for this purpose).

Figure 4, *b* demonstrates that a dark field is formed in a TXM with sample illumination by a hollow cone (a hollow X-ray cone may be produced by capillary optics [19]) by installing annular aperture diaphragm *4* to block unscattered radiation [20]. Another way to form a dark field is to use a condenser with a high numerical aperture (greater than the numerical aperture of zone plate *3* [6,7]). Only the X-ray radiation scattered by a sample reaches the detector in this case (Fig. 4, *a*).

2.2. Laue analyzer method

The studied sample is positioned between the crystals of a double-crystal diffractometer (Fig. 5, *a*). Its first (monochromator) crystal limits the angular and spectral divergence of the primary X-ray beam and forms a wide plane-wave front. The second (analyzer) crystal, which is located between the sample and a detector, serves as an angular filter that cuts out only a narrow angular interval from a beam passing through the sample. Phase gradients present in the sample deflect X-rays locally from the direction of initial propagation. This implies that unrefracted X-rays from the object do no longer propagate in the direction of the transmitted beam.

Two-dimensional refraction-based X-ray imaging with an analyzer has been demonstrated for the first time by Ingal and Belyaevskaya [21,22] (dark-field and bright-field images in these studies were obtained simultaneously).

The greatest phase contrast here is to be expected when the operating point is positioned on the slopes of the rocking curve (points *1, 2* in Fig. 5, *b*) of the analyzer. At the same time, it is impossible to suppress the dynamic background completely in these conditions.

Provided that the absorption is zero and the diffraction is symmetric (the angles between the inward normal to the surface and the directions of propagation of incident and diffracted beams are equal), the intensity of diffracted $I_R(W)$ and transmitted $I_T(W)$ X-ray beams may be written as [8]

$$I_T(W) = \sin^2\left(t\pi\left(1 + W^2\right)^{1/2}/\Lambda\right) / \left(1 + W^2\right), \quad (2)$$

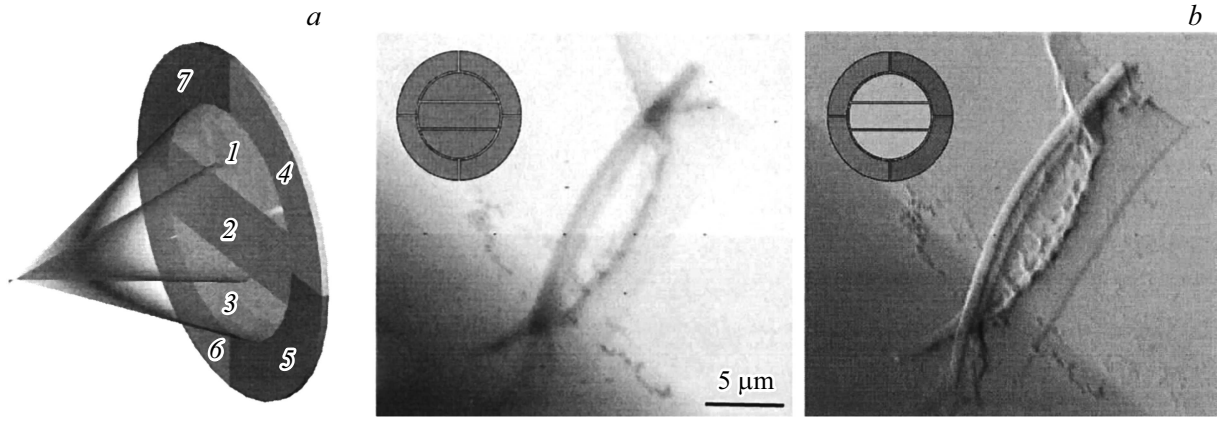

Figure 3. (*a*) Detector with seven active segments [18]. (*b*) Bright-field (left) and dark-field (right) images of a phytoplankton cell [17] (see text).

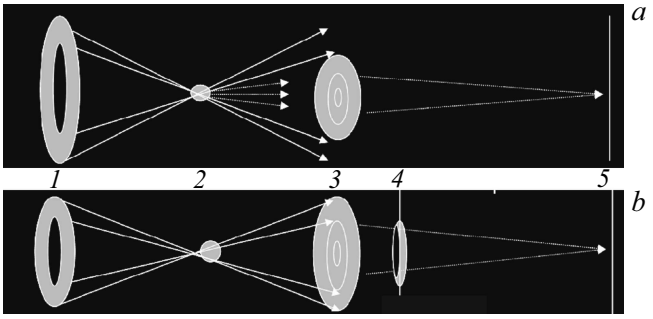

Figure 4. Optical TXM circuits operating in the dark-field mode. *1* — Hollow conical X-ray beam formed by a condenser, *2* — sample, *3* — objective Fresnel zone plate, *4* — ring blocking unscattered radiation, and *5* — detection plane [18].

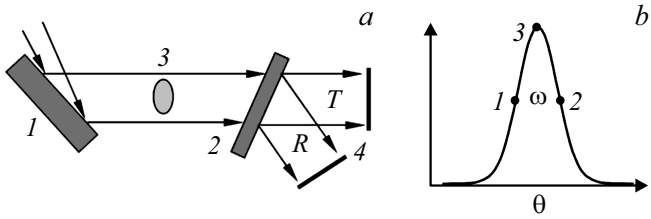

Figure 5. (*a*) Schematic diagram of the Laue analyzer method: *1* — monochromator crystal, *2* — analyzer crystal, *3* — object under study, *4* — detectors, and *T*, *R* — transmitted and diffracted beams that produce dark-field and bright-field images, respectively; (*b*) rocking curve of a single crystal: positioning of the operating point on the slopes (*1, 2*) and at the top (*3*) of the rocking curve (ω is the width of the rocking curve, $\omega = 2C|\chi_{hr}|/\sin 2\theta_B$).

$$I_R(W) = \left\{\cos^2\left[t\pi\left(1+W^2\right)^{1/2}/\Lambda\right] + W^2\right\}/\left(1+W^2\right), \tag{3}$$

$$I_T(W) + I_R(W) = 1, \tag{4}$$

$$\Lambda = \lambda\cos\theta_B/C|\chi_{hr}|, \tag{5}$$

$$\chi_{hr} = -\left(re\lambda^2/\pi V\right)F_{hr}, \tag{6}$$

where t, W, Λ are the analyzer thickness, the deviation of an angle from the exact Bragg condition, and the extinction depth, respectively; $W = 2\Lambda\sin\theta(\Delta\theta_B + \Delta\theta_0)/\lambda$; $\Delta\lambda_B$ is the angle of deviation from Bragg angle θ_B; $\Delta\theta_0$ is the Bragg angle correction for X-ray refraction; χ_{hr} is the real part of the Fourier component of crystal polarizability; polarization factor $C = 1$ for wave field components polarized perpendicular to the scattering plane (σ-polarization) and $C = \cos 2\theta_B$ for components polarized within this plane (π-polarization); V is the unit cell volume; $r_e = e/mc^2$ is the classical electron radius; and F_{hr} is the real part of structural amplitude.

If the operating point, which characterizes the relative angular position of the monochromator and the analyzer, is

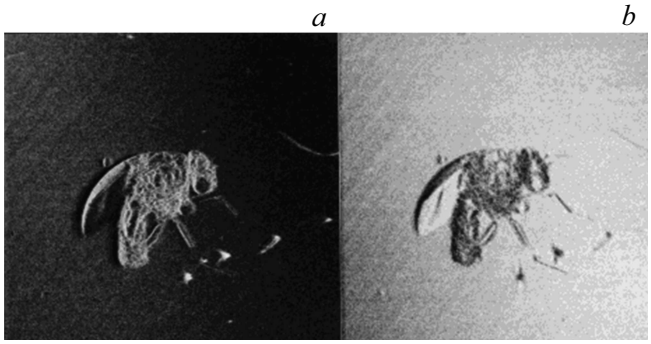

Figure 6. Insect imaged in dark-field (*a*) and bright-field (*b*) modes (the field of view is 5 × 5 mm in size) [8].

at the peak of the rocking curve (i.e., $W = 0$; point *3* in Fig. 4, *b*), formulae (2) and (3) take the following form:

$$I_R(W=0) = \cos^2(\pi t/\Lambda),$$

$$I_T(W=0) = \sin^2(\pi t/\Lambda).$$

Adjusting the energy of the primary beam and the thickness of the analyzer crystal, one may establish the

conditions when $I_R(W=0)=1$ and $I_T(W=0)=0$ (i.e., the intensity of the transmitted beam is virtually equal to zero). This implies that the transmitted beam consists only of scattered X-rays that have changed their trajectory as a result of interaction with the sample. At the same time, since the background is weak (zero), one might expect to obtain high-contrast dark-field images.

An insect imaged in dark-field (Fig. 6, *a*) and bright-field (Fig. 6, *b*) modes is shown in Fig. 6.

Since the wave field propagating in a crystal fills the entire Bormann triangle, a dark-field image with symmetric diffraction undergoes blurring δT: $\delta T = 2t\sin\theta_B$. The resolution reduction may be suppressed by shortening the base of the Bormann triangle (i.e., by thinning the analyzer). A thinner analyzer should thus produce a sharper image. Another way to shorten the base of the Bormann triangle is to reduce angle $2\theta_B$ at its apex. This requires a shorter wavelength and/or a reflection with low Miller indices [23,24].

This method has found applications in medical imaging of bones [25], articular cartilage [26–28], and the mammary gland [29].

3. Indirect multimodal dark-field imaging techniques

However, the X-ray microscopy methods discussed in the previous section and the Laue analyzer method do not allow one to separate the effects of refraction and SAXS. Multimodal X-ray imaging techniques provide an opportunity to separate X-ray absorption, refraction, and scattering patterns in a single experiment. SAXS is manifested in images as local blurring and/or weakening of image intensity, and experimental data need to be processed to retrieve this information.

3.1. Propagation method

Propagation-based imaging [9,30,31], which relies on free-space propagation of spatially coherent X-rays transmitted through a sample and recorded by a detector, is the simplest multimodal X-ray imaging technique.

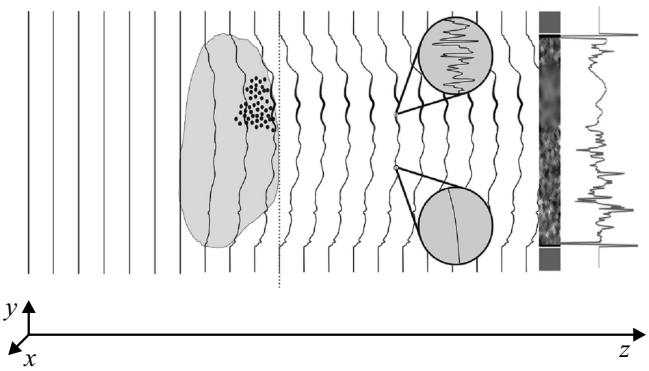

Figure 7. Schematic diagram of propagation of a plane wave field distorted by a sample with an unresolved microstructure [32] (see text).

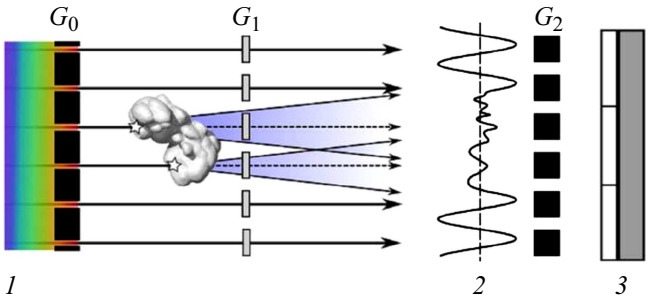

Figure 8. Schematic diagram of dark-field imaging in a Talbot–Lau X-ray interferometer: G_0, G_1, and G_2 — gratings; *1* — polychromatic X-ray radiation; *2* — interference pattern at the output of grating G_1 resulting from SAXS off finely dispersed inclusions (kidney stones, which are marked with asterisks); and *3* — pixel detector [48].

In the wave pattern (Fig. 7), the X-ray wave field undergoes phase shifts in passing through the sample. The phase of the outgoing wave field may be separated into a slowly varying component, which is associated with the spatially resolved sample structure and gives rise to a propagation-based phase-contrast signal, and a rapidly varying component, which is associated with the unresolved microstructure and produces a dark-field signal.

Dark-field effects have traditionally been ignored or considered insignificant in X-ray imaging. In this context, the transport-of-intensity equation (TIE) [33] may be used to model the formation of X-ray intensity images at a detector located behind the sample at distance $z=\Delta$ along the optical axis. This free-space propagation yields intensity bands in the image [30,34] that may be used in phase reconstruction algorithms to obtain quantitative data on the sample [35].

However, if the sample contains an unresolved spatially random microstructure, SAXS will also be present. This additional effect in modeling of paraxial hard X-ray imaging of thin objects may be taken into account with the use of a rigorous theoretical formalism based on wave optical theory [36] or a more general equation than TIE (specifically, the Fokker–Planck equation [37]).

The Fokker–Planck equation may also be regarded as a transport-of-intensity equation with an added diffusion term [15,38]:

$$I(x,y,z+\Delta) \approx \left[1+\Delta^2 D(x,y)\nabla_\perp^2\right] I(x,y,z) - (\Delta/k)\nabla_\perp[I(x,y,z)\nabla_\perp\varphi(x,y,z)]. \quad (7)$$

Here I is the intensity of the monochromatic scalar wave field, φ is its phase, k is the wavenumber ($k=2\pi/\lambda$), $\nabla_\perp=(\partial x,\partial y)$ is the gradient operator in transverse coordinates (x,y), and $\nabla_\perp^2 \equiv \partial^2/\partial x^2+\partial^2/\partial y^2$ is the Laplacian in plane (x,y) perpendicular to optical axis z. The above

expression includes both coherent and diffuse fluxes of energy behind the sample.

Since the measured image blurring L depends on sample–detector distance Δ (formula (2)), two exposures are sufficient to determine the dark-field signal when the Fokker–Planck equation is used. A small propagation distance Δ satisfying the near-field condition ($\Delta \leq 2\pi\xi d/\lambda$, where λ is the wavelength,ξ is the transverse coherence length, and d is the average scattering inhomogeneity size) is recommended for phase reconstruction in the first exposure, since the sample features to be resolved may be blurred by dark-field effects at long propagation distances. In the second exposure, a longer propagation distance, where dark-field effects are visually obvious, is recommended for extraction of the dark-field signal (note that the near-field condition should still be satisfied). The use of three different propagation distances would allow one to determine the phase, absorption, and the dark-field signal separately [32].

Since the dark field is associated with scattering, it depends strongly on the X-ray radiation energy. Therefore, adjustment of the X-ray beam energy is an alternative to changing the distance. The authors of [39] have proposed a concept of dark-field imaging based on the propagation method (with the Fokker–Planck equation) under the assumption that the sample is made of a single material and the dark-field signal varies slowly in space.

Multi-energy reconstruction opens up opportunities for the use of detectors with energy discrimination, making it possible to collect data in a single exposure in the time-resolved mode [39].

A more efficient dark-field signal extraction algorithm for objects mostly consisting of a single material (or several different materials with close ratios of the real part of the complex refraction index to the imaginary one) has been developed recently; this method requires a single image to extract the dark-field signal in 2D imaging. In the case of tomographic imaging, the method requires just one image obtained for each projection angle [9]. The algorithm was applied in mammography to analyze 3D images of five fresh mastectomies containing microcalcifications [40].

3.2. Talbot interferometer

Note that the Talbot interferometer is the instrument that paved the way for widespread application of dark-field imaging [10,41–43].

Talbot has discovered in 1836 [44] that when a primary coherent wave passes through a periodic structure (e.g., a diffraction grating), self-reproduction of its image is observed at distances $d_T = 2mp^2/\lambda$ (p is the grating period, $m = 1, 2, 3\ldots$) behind the structure. This phenomenon is called the Talbot effect, and distance d_T is referred to as the Talbot distance.

A Talbot X-ray interferometer consists of two diffraction gratings G_1 and G_2. The first grating G_1 with period p_1 acts as a beam splitter and causes periodic modulation of the wave front. The period of the Fresnel interference pattern is on the order of a few micrometers and is typically much lower than the detector resolution. Therefore, a second grating G_2 with strongly absorbing lines should be placed in front of the detector. This grating acts as an analyzer, since it converts the positions of interference fringes into intensity values. Grating G_2 with period $p_2 = p_1/\eta$ ($\eta = 1, 2$), which is made of a material that is highly absorbing in the X-ray range, is located in one of the planes of maximum contrast of the interference pattern [45–47].

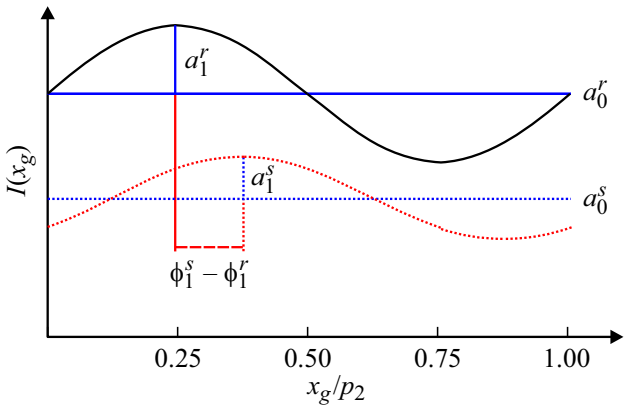

Figure 9. Measured intensity in a detector pixel for the reference scan (superscript r) and the sample scan (superscript s) within one cycle of stepwise phase variation [52].

SR sources and microfocus X-ray tubes satisfy the coherence condition in most cases, but the same is not true for conventional X-ray tubes. In the latter case, one needs to install absorption grating G_0 in front of the source to obtain a phase-contrast image (Fig. 8). This three-grating design is called the Talbot–Lau interferometer. Grating G_0 in it serves to create a series of individual coherent (but mutually incoherent) subsources.

At present, absorption, phase, and dark-field contrast signals may be obtained in phase-stepping measurements [49]. The underlying idea of the method is to estimate local changes in intensity $I(m, n, x_g)$ fluctuations caused by the object and reconstruct images, including a dark-field one, from these several signals [10,50,51]. With one of the gratings moving stepwise in direction x_g perpendicular to the grating line, intensity signal $I(m, n)$ in each detector pixel m, n follows a sinusoidal curve (the so-called phase step curve) (Fig. 9). Only a finite number of steps N_{ps} are performed in a single period p_2. Recorded intensity $I_k(m, n)$ may then be written as a Fourier series:

$$I_k(m, n, x_g) = \sum_i a_i(m, n) \sin(2\pi i k x_g + \varphi_i(m, n))$$

$$\approx a_0(m, n) + a_1(m, n) \sin(2\pi k x_g + \varphi_1(m, n)), \quad (8)$$

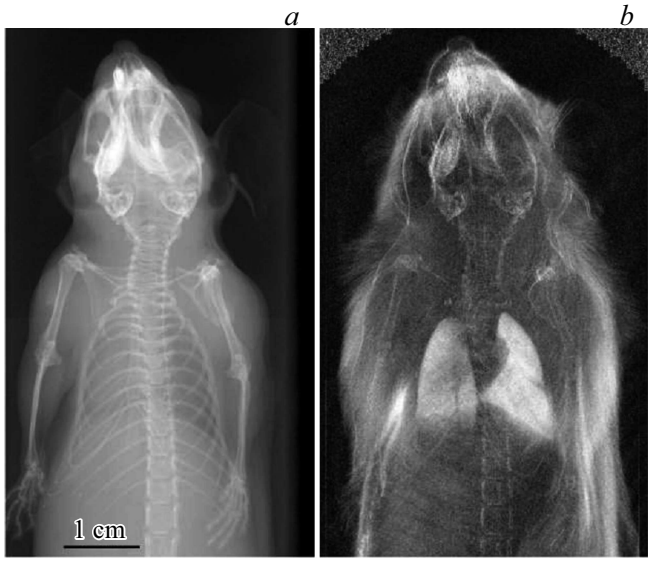

Figure 10. Whole-body *in vivo* X-ray image of a healthy mouse: absorption (*a*) and dark-field (*b*) images illustrating that tissues, such as lungs and fur, generate a SAXS signal [55].

where a_i are amplitude coefficients, φ_i are the corresponding phase coefficients, $k = 2\pi/p_2$, and p_2 is grating period G_2. Coefficients a_0, a_1, and φ_1 are retrieved from the obtained phase step curve I_k dataset via fast Fourier transform [10,47] and are used to calculate absorption, phase-contrast, and dark-field images. This requires at least three measurements ($N_{ps} \geq 3$) both without a sample (reference measurement) and with a sample introduced into the beam; the typical number of measurements falls within the range of 5–11 [10]. If we define the visibility of the phase step curve as $v(m, n) = a_1/a_0$, dark-field signal V is given by

$$\begin{aligned} V(m,n) &= v^s(m,n)/v^r(m,n) \\ &= a_1^s(m,n)a_0^r(m,n)/a_0^s(m,n)a_1^r(m,n), \end{aligned} \tag{9}$$

where superscripts r and s correspond to measurements without and with a sample.

Experiments in mice [53,54] have revealed that healthy lung tissue exhibits a very strong dark-field signal generated by SAXS at numerous air–tissue interfaces typical of the microarchitecture of normal lung parenchyma. Lungs do indeed stand out as the organ that generates the strongest dark-field signal in whole-body X-ray images of mice (Fig. 10) [55]. Owing to a close relationship between the alveolar structure and lung function, dark-field lung imaging is of great importance in respiratory medicine and may help diagnose and treat lung diseases [56–58].

At present, lung imaging is probably the most promising clinical application of dark-field X-ray imaging [59].

Other potential clinical applications of Talbot interferometers for dark-field X-ray imaging include detection of foreign bodies in food [60,61], differentiation of kidney stones [48], examination of bone structures [62,63], and mammography. In the context of diagnosis of multifocal tumor growth, dark-field mammography is superior to standard breast imaging methods, providing better resolution of small calcified tumor nodules and demarcation of tumor boundaries [64–66].

Dark-field imaging has several industrial applications, such as the detection of voids, cracks, or delaminations [66,67].

A Talbot interferometer may also be used for dark-field computed tomography [68–70].

If a sample scatters X-rays purely isotropically, its dark-field signal is independent of orientation. However, if scattering is partially anisotropic, the signal formation is orientation-dependent, and the signal is thus much harder to reconstruct. One-dimensional (1D) grating interferometry is the method that is used most often for retrieving a directional dark-field signal, since diffuse scattering is most pronounced in the direction orthogonal to grating lines.

Two-dimensional orientation of the microstructure in a sample may be calculated using several dark-field images obtained in phase-stepping measurements at different angular positions of the sample that is rotated about the beam propagation direction [68,69]. The method of anisotropic dark-field X-ray tomography [71–74], which is based on the works of Malecki et al. [75] and Vogel et al. [76], was proposed for tomographic reconstruction of an anisotropic SAXS signal.

The dark-field signal formation is governed by three parameters: the X-ray radiation direction, the dark-field sensitivity direction, and the anisotropic microstructure orientation. The authors of [77] have proposed a very general model in which all three quantities are regarded as arbitrary three-dimensional vectors. It provides an opportunity to model not only a system with a parallel beam and a perpendicular sensitivity direction, but also arbitrary data collection geometry. In contrast to the existing 2D projection models with a predetermined image trajectory, this model allows for arbitrary 3D scanning trajectories (e.g., a helical one).

To obtain signals in multiple orientations, one needs to rotate samples or one-dimensional gratings about the beam propagation direction, which is time-consuming if multiple directions are to be scanned in the study of an unidentified sample. A two-dimensional (2D) interferometer with two-dimensional gratings may cover up to four dark-field signal directions without sample rotation [78], but raster scanning in each direction is still required.

Fiber-reinforced polymers are now used widely in the automotive industry and many other industrial sectors. The orientation of fibers is crucial to enhancing the mechanical strength of parts. Owing to scattering anisotropy, dark-field contrast allows one to detect local fiber orientations in polymers [60,70–82]. The determination of orientation of fibers in cardboard was reported in [83], and directional

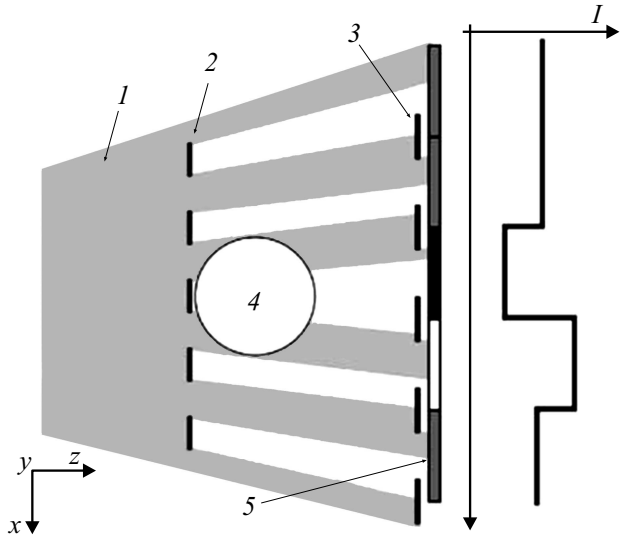

Figure 11. Schematic diagram of the edge illumination method: *1* — primary X-ray beam, *2* — sample mask, *3* — detector mask, *4* — sample, and *5* — detector pixel [90].

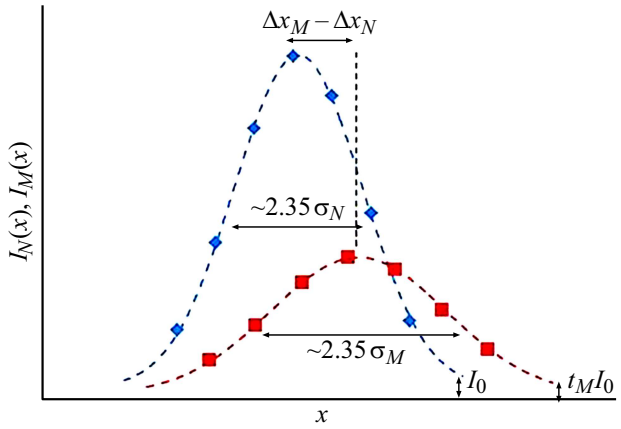

Figure 12. Example light curves measured with (squares) and without (diamonds) a sample. The introduction of a sample into the beam leads to a reduction in intensity, lateral shifts, and broadening of the curve, which allow one to extract absorption, refraction, and SAXS signals, respectively [91] (see text).

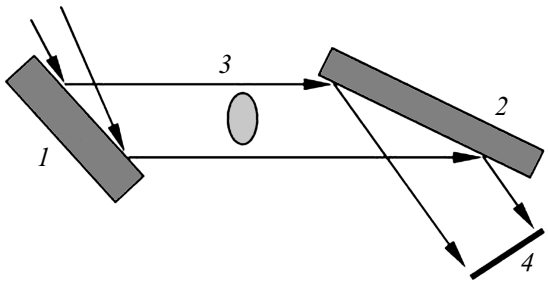

Figure 13. Diagram of the experimental setup: *1* — monochromator, *2* — analyzer crystal, *3* — sample, and *4* — detector.

dark-field X-ray imaging was used in [84] to analyze archaeological finds.

Diagnosis and monitoring of treatment of osteoporosis is a major public health issue, since osteoporosis is associated with fragility fractures. It is characterized not only by a loss of bone mineral density, but also by a reduction in bone quality, which includes deterioration of the trabecular microstructure. The correlation between X-ray directional radiography and the trabecular microstructure was investigated in [85–87]. Thus, changes in the trabecular bone structure due to osteoporosis or osteoporosis-related therapy may be detected much earlier and with a sensitivity higher than the one offered by conventional X-ray methods.

3.3. Edge illumination method

Both multimodal methods discussed above are interferometric in nature; i.e., they require the use of coherent radiation, which is often associated with scattering intensity losses.

The edge illumination method is a non-interferometric technique that has been demonstrated for the first time at synchrotron sources in the late 1990s [88]. It has later been adapted to commercially available X-ray sources, which have large focal spot sizes, without collimation. A typical experimental setup consists of two periodic absorbing structures that are often called masks and are placed in front of the sample and the detector, respectively (Fig. 11). Sample mask *2* splits incoming X-ray beam *1* into a series of individual beams separated by mask period p_1, while the absorbing edges of detector mask *3* are positioned so that each individual beam may hit the boundary between two pixels. The masks are designed so that their periods match the detector pixel size. Therefore, a detector pixel is sensitive to the beam displacement caused by X-ray beam refraction [89].

As the sample mask moves along the x axis and the fraction of a beam reaching the detector changes, the illumination of each pixel is modulated by the so-called illumination curve.

At least three intensity projections are needed to separate absorption, phase, and SAXS signals in a system with edge illumination. Each of these projections is obtained with different shifts of the sample mask relative to the detector mask, which correspond to exposures at different points on the illumination curve (Fig. 12).

The first stage of dark-field signal extraction is the measurement of the illumination curve without a sample. The illumination curve is then measured with the sample introduced into the beam. The obtained two curves are fitted with Gaussians, and the curve with the sample $(I_M(x))$ is then compared with the corresponding curve $(I_N(x))$ obtained without the sample [91]:

$$I_N(x) = t_N \left(2\pi\sigma_N^2\right)^{-1/2} \exp\left[-(x-\Delta x_N)^2/2\sigma_N^2\right] + I_0, \quad (10)$$

$$I_M(x)=t_M\left\{t_N\left(2\pi\sigma_M^2\right)^{-1/2}\exp\left[-(x-\Delta x_M)^2/2\sigma_M^2\right]+I_0\right\}. \quad (11)$$

Absorption of X-rays leads to a reduction in the area of the Gaussian, refraction induces a change in the position of its center, and SAXS alters the width of the Gaussian [92].

A comparison between $I_M(x)$ and $I_N(x)$ allows one to extract absorption t_M, refraction $\Delta x_M - \Delta x_N$, and SAXS $\sigma_M^2 - \sigma_N^2$ signals separately by measuring the illumination curve [92,93].

3.4. Bragg analyzer method

The Bragg analyzer method [12,94–98] gained widespread use in biomedicine [99,100] and materials science [101].

Just as in the Laue analyzer method, the studied sample is positioned between the crystals of a double-crystal diffractometer [100,102] (Fig. 13). Its first (monochromator) crystal *1* limits the angular and spectral divergence of the primary X-ray beam. The second (analyzer) crystal *2*, which is located between sample *3* and detector *4*, act as an angular filter.

When the operating point is positioned on the slope of the rocking curve, the maximum image contrast dynamics is achievable: the narrower the rocking curve is, the higher is the sensitivity of the method to phase changes.

Several algorithms for efficient separation of absorption, refraction, and SAXS signals and their accurate quantitative assessment have been proposed [99,103].

A three-image algorithm providing a simple way to represent three effects in three different parametric images was detailed in [104,105].

Let $\theta_j\{j \in [1, 3]\}$ be three different positions of the operating point on the rocking curve, which yield three different images $I_j = I(\theta_j)$ of one and the same object. A system may be formed from three equations written for each image I_j:

$$I_j = (I_R/2)\left[2R_j + 2R'_j\Delta\theta_R + R''_j(\Delta\theta_R)^2 + R''_j\sigma^2\right], \quad j \in [1, 3], \quad (12)$$

where R_j, R'_j, and R''_j correspond to the values of the rocking curve and its first and second derivatives calculated at angular position θ_j. The solution of system (12) yields three parametric images: absorption image I_R, refraction image $\Delta\theta_R$, and dark-field image σ^2 (Fig. 14).

If two images are obtained from each slope of the rocking curve (Fig. 5, *b*), where $R''_1 = R''_2 = 0$ and $I_1 = I_2$ (Fig. 5, *b*), then the solution of system (12) yields the SAXS signal equation:

$$\sigma^2 = [I_2/I_R - R_2 - R'_2(\Delta\theta_R)]/R''_2 - (\Delta\theta_R)^2. \quad (13)$$

In fact, if I_3 corresponds to the position of the operating point at the peak of the rocking curve ($R'_3 = 0$), Eq. (13) is simplified even further:

$$\sigma^2 = 2(I_2/I_R - R_2)/R''_2 - \Delta\theta_R^2. \quad (14)$$

It should be noted that the method provides quantitative information in the angular range of validity of the Taylor expansion (i.e., at angles of refraction and scattering on the order of several μrad, which are significantly smaller than the width of the rocking curve). If the scattering angle exceeds this limit, the algorithms tend to fail, and saturation is observed [105]. A novel analytical algorithm called Gaussian Generalized Diffraction Enhanced Imaging (G^2DEI) [106], which is based on three images, was proposed as a means to overcome these constraints. This algorithm has the capacity to operate in a wider range of refraction and scattering angles (exceeding ten μrad) that is needed, e.g., in studies of biological objects.

In 2003, Pagot et al. [107], Oltulu et al. [108], and Wernick et al. [109] have independently developed statistical methods that allow one to perform pixel-by-pixel reconstruction of the analyzer rocking curve by combining conveniently multiple images corresponding to different segments of the rocking curve. The authors of [109] called this method „multiple-image radiography“ (MIR). It consists in obtaining two series of N ($N \geq 3$) images in different positions of the analyzer crystal with and without a sample, respectively. The „reference“ (obtained without the sample) and „object“ (obtained with the sample) rocking curves are then compared.

The procedure of MIR reconstruction in application to the Laue analyzer has been proposed and demonstrated in [110]. Simultaneous recording of transmitted and diffracted images of a sample with a large field of view allows for significant simplification and acceleration of data acquisition and makes it possible to reduce the radiation dose, which is important for biological research [110–112].

However, the use of statistical methods extends the imaging time and raises the X-ray dose absorbed by a sample, since one needs to obtain more images. Another approach to extraction of relevant parameters consists in fitting a functional form to the measured rocking curves at a limited number of operating point positions. This may require significant computational resources, but allows for flexible post-processing of the data. At first glance, a Gaussian is an obvious choice of a fitting function [113]. However, it turned out that the Gaussian approximation cannot reproduce correctly both the maximum of the rocking curve and its tails [101,114].

Among various tested rocking curve fitting functions (such as Pearson VII [115]), the pseudo-Voigt (PsdV) function was found to be the best fit to experimental data. The Voigt function is a convolution of Gaussian and Lorentzian functions, while the PsdV function is a close approximation of it provided by a simpler weighted sum of these two functions. It was demonstrated [114] that a minimum of five operating points are needed for a good fit and that the diffuse part (SAXS) is characterized by Lorentzian tails (i.e., it can extend to angles exceeding

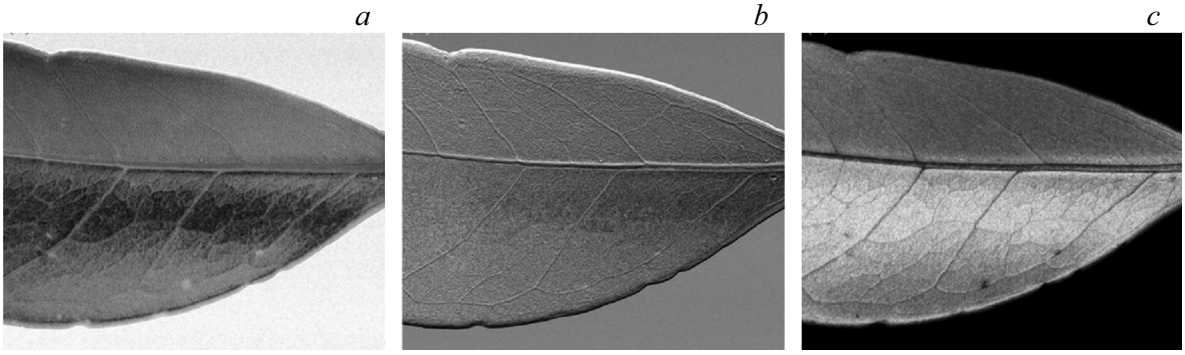

Figure 14. Parametric images of a leaf: (a) I_R (absorption), (b) $\Delta\theta_R$ (refraction), and (c) σ^2 (SAXS) [104].

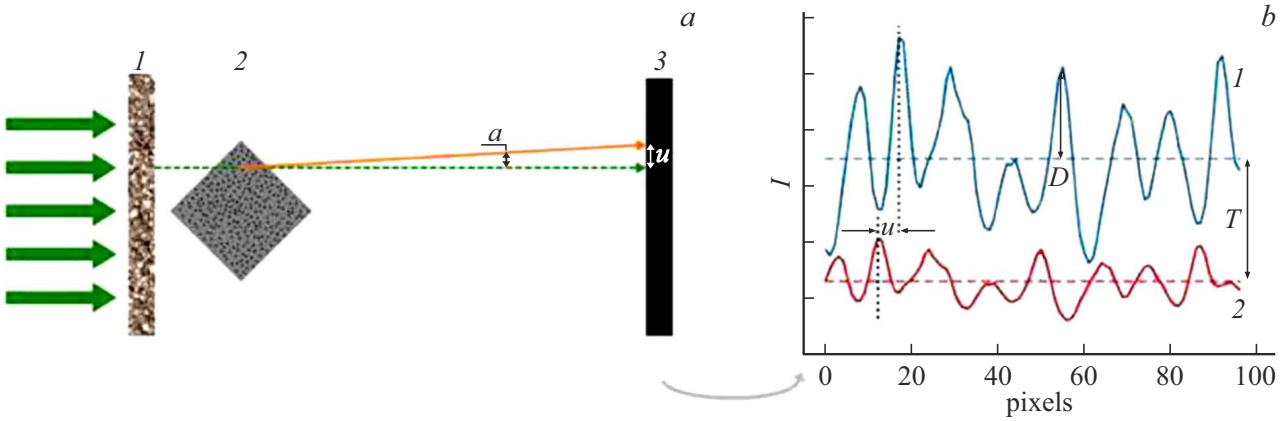

Figure 15. (a) Schematic diagram of an X-ray speckle imaging experiment: *1* — diffuser, *2* — sample, and *3* — pixel detector. (b) Linear plot of the reference (curve *1*) intensity and the intensity with a sample introduced into the X-ray beam (curve *2*). The plot reveals an intensity drop (dashed horizontal lines) due to absorption $A = (1 - T)$, shift u due to X-ray refraction by angle α, and amplitude reduction D (after correction for X-ray absorption) due to SAXS [13].

the width of the rocking curve by a factor of more than 10).

3.5. Speckle-based method

When an object consisting of elements with a high spatial frequency is introduced into a coherent or partially coherent photon beam, a speckle pattern is generated by a combination of multiple waves of the same frequency with different phases and amplitudes. In the near field, the speckle size does not depend on the distance to the phase membrane or the X-ray radiation energy [116,117]. This unique property enables the use of near-field speckles for the examination of inhomogeneous systems [118].

The visibility of speckle grains in images and their size are the criteria for identifying a fine speckle generator. In practice, the grain size should be chosen so that it covers several image pixels (< 10 pixels) and has a minimum contrast of 0.1 (contrast is defined here as the standard deviation from the mean intensity). Depending on the photon energy and the detector type used, various options such as granular materials, sandpaper, or filters (e.g., cellulose with micrometer pore sizes) may turn out to be suitable [119].

As for the X-ray radiation source, the demands of the speckle-based method are moderate. X-ray speckle imaging may be performed with the use of polychromatic laboratory sources [120], and the requirements as to temporal coherence are low [121].

A basic setup for speckle imaging is shown in Fig. 15, a [13]. An X-ray beam incident on diffuser *1* (e.g., a piece of sandpaper) produces a random reference speckle pattern in the detector plane. When sample *2* is introduced into the beam, the speckle pattern is modulated by its presence, and the resulting interference pattern is recorded by a detector. Modulation manifests itself in three ways (see Fig. 15, b): speckles are shifted in horizontal direction x and in vertical direction y by vector $\mathbf{u} = (u_x, u_y)$ due to refraction in the sample; the mean intensity changes due to absorption; and the pattern visibility (i.e., the amplitude with absorption taken into account) is reduced due to SAXS.

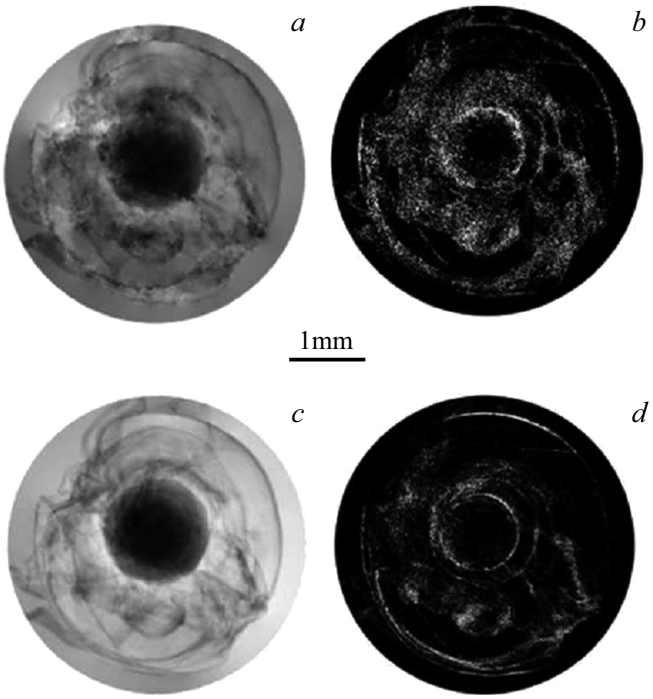

Figure 16. (*a*) Phase-contrast and (*b*) dark-field images of the eyeball of a fish (sprat) obtained by speckle tracking; (*c*) and (*d*) similar images obtained by speckle scanning in one direction [127] (see text).

Refraction angle $\alpha = (\alpha_x, \alpha_y)$, which is related to the differential phase shift, transmission T (or absorption $A = 1 - T$), and dark-field signal D may be reconstructed quantitatively from these effects. Reconstruction is performed pixel by pixel in real space with the use of various analysis methods.

X-ray speckle imaging was first implemented in the single-shot mode in the form of X-ray speckle-tracking (XST), which requires only one reference image with a diffuser and one image with a diffuser and a sample in the beam [122,123].

The measurement concept relies on a physical model of speckle interference in the detector plane that takes into account the pattern modulation by a sample. For a given pixel (x, y), interference pattern I may be characterized in terms of reference interference pattern I_0 modulated in intensity, amplitude, and position by the properties of the sample [13]:

$$I(x, y) = T(x, y)[\hat{I}_0 + D(x, y)(I_0(x + u_x, y + u_y) - \hat{I}_0)]. \quad (15)$$

Here, $\hat{I}_0$ is the mean intensity of the reference pattern and $T(x, y)$ is the local transmission through the sample that reduces the intensity of the speckle pattern. Amplitude $(I_0(x + u_x, y + u_y) - \hat{I}_0)$ of the reference pattern is reduced by factor $D(x, y)$ corresponding to the local dark-field signal.

Refraction in the sample is characterized by quantities u_x and u_y corresponding to the displacement of the interference pattern in horizontal and vertical directions, respectively. To reconstruct the image, least-squares minimization of Eq. (15) is performed pixel by pixel using the sum over pixels in analysis window w around the (x_0, y_0) pixel [13,120]:

$$L = \sum_{i=-M}^{M} \sum_{j=-M}^{M} w(x_i, y_j) \{I(x_i, y_j) - T(x_i, y_j)[\hat{I}_0 + D(x_i, y_j)(I_0(x_i + u_x, y_j + u_y) - \hat{I}_0)]\}^2. \quad (16)$$

Minimization of function L yields multimodal image signals u_x, u_y, T, and D [120]. A fine reconstruction may be obtained if window size w exceeds the average speckle size.

The main advantage of the XST implementation is fast image acquisition, which makes it suitable for dynamic imaging and *in vivo* studies. It has been demonstrated that a single image with an exposure of less than a second at a synchrotron source is sufficient for reconstruction [124]. In addition, XST, unlike speckle scanning, does not require any special equipment.

The main disadvantage of XST is its limited spatial resolution specified by the analysis window size, which must exceed the speckle size. The ultimate limit of resolution of this operating mode is the speckle size.

The X-ray speckle scanning (XSS) mode is better suited for applications where high resolution is more important than fast image acquisition. It may be regarded as a generalization of X-ray grating interferometry in the phase-stepping mode [125]. However, unlike Fourier analysis performed in X-ray grating interferometry, speckle scanning data are analyzed in real space.

The speckle scanning mode was implemented in experiments [126] in two different ways (with two-dimensional and one-dimensional scanning). This method requires that the speckle pattern be shifted by a known constant step. However, unlike the XST approach where several pixels in the analysis window contribute to reconstruction of the signal of a single pixel, the step mode allows for pixel-by-pixel analysis. This provides a much higher resolution (down to the pixel size), which is the main advantage of XSS.

Figure 16 presents phase-contrast and dark-field images of the eyeball of a fish (sprat). The quality of phase-contrast images obtained by speckle tracking (Fig. 16, *a*) is low due to poor spatial resolution. In contrast, the speckle scanning method provides high-quality images with a significantly improved spatial resolution that reveal all the fine details of the eyeball (Fig. 16, *b*). Fine details are also seen clearly in the dark-field image in Fig. 16, *c* (cf. Fig. 16, *b* [127]).

The use of two orthogonal 1D scans instead of a full 2D scan of the diffuser was proposed as a way to reduce the number of acquired images in the case of small speckle shifts. In this mode, which is called 1D XSS,

the diffuser moves in one direction only (horizontally or vertically) in equally spaced steps that are much smaller than the average speckle size and on the order of the pixel size. This is done without a sample and with a sample in the beam. The transmission and dark-field signals are reconstructed in the same way as in 2D XSS and XST (i.e., by monitoring local changes in the mean intensity and visibility for each pixel). The image acquisition time in 1D XSS is much shorter than in the 2D XSS approach. However, several tens of frames are needed for successful image reconstruction. Most experimental 1D XSS implementations discussed in literature [13] utilized a set of 60 diffuser steps; a minimum of 40 steps was reported. The sensitivity of reconstructed images in two orthogonal directions is nonuniform [13]. It normally decreases in the scanning direction due to the dependence on the effective pixel size and on the step size for the scanning direction. One-dimensional XSS may be used efficiently when a preferred direction of interest is known and signals of the sample in the other direction are less important [13].

The 1D XSS approach requires a significantly smaller number of diffuser steps than 2D XSS, but this comes at the cost of reduced sensitivity in the direction orthogonal to the scan axis. In addition, for the reconstruction to be successful, it is advisable to use a few more diffuser positions.

There are several important limitations to the implementation of speckle-based imaging in the XST and XSS modes. While the spatial resolution of XST is fairly limited, XSS modes require a large number of frames. One-dimensional XSS is characterized by a difference in sensitivity in horizontal and vertical directions and reduced resolution. Several efforts were mounted to develop experimental implementations that provide a compromise between the advantages and disadvantages of classic XST and XSS modes. Two approaches have been proposed towards that end: X-ray speckle vector tracking (XSVT) [128] and unified modulated pattern analysis (UMPA) [120]. In contrast to XSS, these advanced methods allow one to choose a random diffuser position, and the step size must be significantly larger than the speckle size. Thus, step movement of the diffuser may be less precise, which also makes the setup less expensive. However, these movements still need to be accurate and reproducible to ensure that sample and reference images are acquired at the same diffuser positions. The required number of steps is much smaller than the one in XSS experiments; therefore, the scanning time is reduced.

In the XSVT method, the signal at each pixel is regarded as a vector composed of intensities measured in all diffuser positions [128]. The dark-field signal is extracted from the ratio of standard deviations of speckle vectors with and without a sample in the beam. Images are reconstructed based on the correlation of speckle vectors [129]. The XSVT method allows one to reduce significantly the total number of sample exposures while maintaining the accuracy of the dark-field signal.

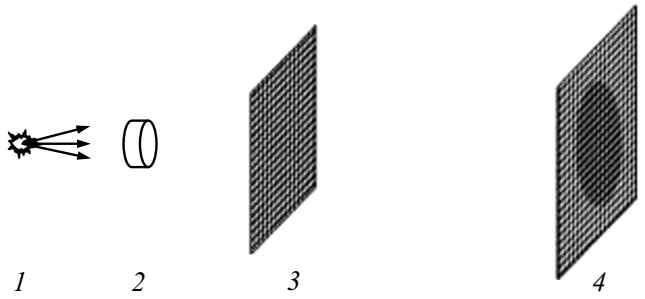

Figure 17. Single-grid imaging device. It features X-ray tube *1*, sample *2*, absorption grid *3*, and X-ray camera *4* [14].

In UMPA, images are recorded with several (n) random positions of the diffuser. This model was first proposed for the XST mode [120]. Equation (15) is valid in UMPA for each interference pattern in diffuser position n. In the process of minimization of function L (Eq. (16)), summation is now performed not only over all pixels in window w, but also over all n diffuser positions [13]. The authors of [130] have demonstrated the feasibility of application of UMPA for extraction of the directional SAXS signal.

In both XSVT and UMPA, the use of an analysis window around the reconstructed pixel allows one to reduce significantly the number of obtained frames by adding information from surrounding pixels. The typical analysis window is just a few pixels in size, inducing a moderate reduction in spatial resolution. However, the choices of the number of steps and the window size are always interrelated. Larger windows normally allow one to use fewer diffuser steps, but reduce spatial resolution; in turn, the use of more diffuser positions allows for high-resolution imaging with a small analysis window at the expense of long acquisition times and high irradiation doses.

Quantitative dark-field tomography has been implemented successfully with XST [120] and 1D XSS [127]. However, in view of the authors of [129], the XSVT method is particularly well-suited for multimodal tomography. Without any a priori assumptions about the sample, it does indeed ensure three-dimensional visualization of the dark-field signal, and the spatial resolution of images is limited only by the properties of the detector used.

Pavlov et al. [131,132] have developed the multimodal intrinsic speckle tracking (MIST) method for imaging of transparent objects that combines a Fokker–Planck description of paraxial X-ray optics [38] with the geometric flow formalism for X-ray speckle tracking [133]. The method was extended to an absorbing object in [134]. The MIST formalism requires only two sets of projection data for two different transverse mask positions (on the assumption that this method may be suited to

clinical applications where radiation dose needs to be minimized).

The authors of [135] used six transverse mask positions to optimize the signal-to-noise ratio. However, when the same approach was implemented with a smaller number of mask positions, the results agreed well with those reported by Pavlov et al. [131,132], demonstrating that two mask positions are sufficient to reconstruct the SAXS signal. The case of rapid variations of the diffuse field in the object was considered in [136]. This improves the quality of solution of the inverse problem.

The MIST method has an advantage in requiring fewer images (and, consequently, less computation time) at the expense of reduced generality. This distinguishes it from, e.g., the UMPA method [137].

It is trivial to extend the MIST method to the more general case of a „directional dark field." For this purpose, one may substitute scalar dimensionless diffusion coefficient $D(x, y)$ with a second-rank diffusion tensor. Equation (15) is then generalized by the following anisotropic Fokker–Planck equation for paraxial X-ray imaging in the presence of both coherent and diffusive energy flow channels [15,132,137]:

$$\begin{aligned} I(x, y, z + \Delta) \approx{}& I(x, y, z) - (\Delta/k)\nabla_{\perp} \\ &\times [I(x, y, z)\nabla_{\perp}\varphi(x, y, z)] \\ &+ \Delta^2[D_{xx}(x, y)\partial^2/\partial x^2 I(x, y, z) \\ &+ D_{yy}(x, y)\partial^2/\partial y^2 I(x, y, z) \\ &+ 2D_{xy}(x, y)\partial^2/\partial xy I(x, y, z)]. \end{aligned} \quad (17)$$

3.6. Single-grid imaging method

Single-grid imaging [14,138] is a technique of X-ray imaging with an absorption grid (Fig. 17) that is introduced into the illuminating beam at a certain distance from a detector and forms a reference image. A sample is then introduced into the beam near the grid. Under X-ray illumination, it distorts and blurs the grid pattern in accordance with the phase and SAXS properties of the sample, respectively [14,138,139].

As the name suggests, single-grid imaging requires only one optical element (grid) and does not require calibration or alignment in preparation for data acquisition. The detector pixel must be smaller than the grid period to resolve fully the intensity pattern formed by the grid. The grid may be replaced by any object producing a high-visibility intensity pattern (e.g., a piece of sandpaper), in which case the method is known as speckle-based imaging.

The projection image of the object is modulated by the periodic grid, and the Fourier spectrum of the projection image becomes a convolution of the grid spectrum and the object spectrum. As a result, it contains a strong primary peak near zero spatial frequency and at least two strong harmonic peaks corresponding to the grid period. The inverse Fourier transform of regions around these peaks yields the primary image and two complex conjugate harmonic images. Since the components with a high spatial frequency are attenuated more profoundly by scattering than those with a low spatial frequency, the ratio between harmonic and primary images yields the SAXS image [140].

This method assumes that the grid image is uniform in period throughout the image (especially for quantitative searching).

As an alternative, the grid image distorted by the sample may be compared with the reference image using the method of local cross-correlation around each pixel [138,139], since Fourier analysis may yield erroneous results when the grid frequency overlaps with the sample microstructure frequency [138]. The spatial mapping method may also provide finer spatial resolution than Fourier analysis [139], since windows are compared in it on a pixel-by-pixel basis without focusing on just a small Fourier space region. The dark-field signal is given by [141,142]

$$D = \exp\left(-\pi^2\Delta^2\theta^2/2p^2\right), \quad (18)$$

where Δ is the sample–detector distance, θ is the „SAXS fan" expansion angle (Fig. 1), and p is the grid period. Equation (18) characterizes the SAXS signal variation with propagation distance, which may be „fitted" to SAXS signals measured at several different distances Δ to determine accurately the effective scattering angle and the modeled sample microstructure [141].

4. Conclusion

X-ray dark-field imaging is a promising method for examination of a wide class of objects. Particular hope is invested in its medical applications and, in particular, its introduction into clinical practice.

It follows from the above that direct suppression of the dynamic background in dark-field imaging may be performed in several ways:

(1) by direct blocking of X-rays unscattered by a sample (X-ray microscopy method);

(2) by orienting the direct beam of X-ray radiation away from a detector (X-ray microscopy method);

(3) by minimizing the dynamic background intensity through interference of X-rays in the crystal (Laue analyzer method). This requires selecting the optimum thickness of the analyzer crystal.

X-rays propagating in a non-crystalline object undergo absorption, refraction, and small-angle scattering. Unfortunately, the Laue analyzer and X-ray microscopy methods do not allow one to separate phase contrast from the contrast produced by SAXS. At the same time, multimodal indirect X-ray methods (Talbot interferometer and propagation-based, edge illumination, Laue analyzer, speckle-based,

and single-grid methods) allow for the separation of all three contrasts and, consequently, are suitable for dark-field imaging.

These methods differ in optical circuit diagrams, data collection and processing techniques, and experimental limitations.

The positive and negative qualities of multimodal methods have been discussed extensively in literature (see, e.g., [143–146]).

Propagation- and analyzer-based imaging techniques require highly coherent sources (primarily transverse coherence for propagation-based imaging and longitudinal coherence for imaging with a Bragg analyzer). In addition, imaging with a Bragg analyzer requires precise alignment and is time-consuming when laboratory sources are used. Propagation-based imaging is characterized by a very simple optical design, but the required source coherence makes it difficult to use in clinical settings.

Grating interferometry, edge illumination, and speckle- and grid-based imaging were proven to be feasible with laboratory sources; however, the Talbot interferometer and edge illumination methods require meticulous alignment and are sensitive to only one scattering direction, which results in poor performance in terms of noise power in tomographic reconstruction. In addition, the presence of numerous optical elements in Talbot interferometer and edge illumination setups often translates into long data acquisition times. In contrast, speckle- and grid-based imaging experiments are easy to set up with account for scattering in two directions. Despite their limited sensitivity, speckle- and grid-based imaging methods have the advantage of simplicity of implementation, which may facilitate dark-field imaging in clinical settings with a gantry rotating around a sample or a patient [146]. At the same time, despite the complexity of adjustment, time costs, and the need for suppression of artifacts [147–149], it is the Talbot interferometer that is already being used successfully in clinical diagnostic setups [150–152].

Acknowledgments

This study was carried out under the state assignment of National Research Center „Kurchatov Institute."

References

[1] S.H. Gage. Trans. Am. Microsc. Soc., **39** (2), 95 (1920). DOI: 10.2307/3221838
[2] A. Yaroshenko, K. Hellbach, M. Bech, S. Grandl, M.F. Reiser, F. Pfeiffer, F.G. Meinel. Curr. Radiol. Rep., **2** (7), 57 (2014). DOI: 10.1007/s40134-014-0057-9
[3] S. Senck, M. Scheerer, V. Revol, B. Plank, C. Hannesschlager, C. Gusenbauer, J. Kastner. Compos. Part A: Appl. Sci. Manuf., **115**, 206 (2018). DOI: 10.1016/j.compositesa.2018.09.023
[4] B.K. Blykers, C. Organista, M. Kagias, F. Marone, M. Stampanoni, M.N. Boone, V. Cnudde, J. Aelterman. J. Imaging, **8** (10), 282 (2022). DOI: 10.3390/jimaging8100282
[5] E.A. Miller, T.A. White, B.S. McDonald, A. Seifert. IEEE Trans. Nucl. Sci., **60** (1), 416 (2013). DOI: 10.1109/TNS.2012.2227803
[6] S. Vogt, H.N. Chapman, C. Jacobsen, R. Medenwaldt. Ultramicroscopy, **87** (1-2), 25 (2001). DOI: 10.1016/s0304-3991(00)00065-6
[7] G.-C. Yin, F. Duewer, X. Zeng, A. Lyon, W. Yun, F.-R. Chen, K.S. Liang. Proc. SPIE, **6317**, 631703 (2006). DOI: 10.1117/12.680216
[8] M. Ando, A. Maksimenko, H. Sugiyama, W. Pattanasiriwisawa, K. Hyodo, C. Uyama. Jpn. J. Appl. Phys., **41** (9A), L1016 (2002). DOI: 10.1143/JJAP.41.L1016
[9] T.E. Gureyev, D.M. Paganin, B. Arhatari, S.T. Taba, S. Lewis, P.C. Brennan, H.M. Quiney. Phys. Med. Biol., **65** (21), 215029 (2020). DOI: 10.1088/1361- 6560/ abac9d
[10] F. Pfeiffer, M. Bech, O. Bunk, P. Kraft, E. Eikenberry, C. Brönnimann, C. Grünzweig, C. David. Nat. Mater., **7**, 134 (2008). DOI: 10.1038/nmat2096
[11] A. Olivo, R. Speller. Appl. Phys. Lett., **91** (7), 074106 (2007). DOI: 10.1063/1.2772193
[12] V.A. Bushuev, A.A. Sergeev. Tech. Phys. Lett., **24** (11), 851 (1998). DOI: 10.1134/1.1262290.
[13] M.-C. Zdora. J. Imaging, **4** (5), 60 (2018). DOI: 10.3390/jimaging4050060.
[14] H.H. Wen, E.E. Bennett, R. Kopace, A.F. Stein, V. Pai. Opt. Lett., **35** (12), 1932 (2010). DOI: 10.1364/OL.35.001932
[15] D.M. Paganin, D. Pelliccia. Adv. Imag. Electron Phys., **218**, 63 (2021). DOI: 10.1016/bs.aiep.2021.04.002
[16] V.V. Lider. Phys. Usp., **60** (2), 187 (2017). DOI: 10.3367/UFNe.2016.06.037830.
[17] B. Hornberger, M.D. de Jonge, M. Feser, P. Holl, C. Holzner, C. Jacobsen, D. Legnini, D. Paterson, P. Rehak, L. Strüder, S. Vogt. J. Synchrotron Rad., **15** (4), 355 (2008). DOI: 10.1107/S0909049508008509
[18] M. Feser, T. Beetz, M. Carlucci-Dayton, C. Jacobsen. AIP Conf. Proc., **507** (1), 367 (2000). DOI: 10.1063/1.1291173
[19] V.V. Lider. Opt. Spectrosc., **130** (14), 2156 (2022). DOI: 10.61011/EOS.2024.04.58889.127-24.
[20] H. Takano, K. Yokota, S. Aoki. Jpn. J. Appl. Phys., **38** (12A), L1485 (1999). DOI: 10.1143/JJAP.38.L1485
[21] V.N. Ingal, E.A. Beliaevskaya. J. Phys. D: Appl. Phys., **28** (11), 2314 (1995). DOI: 10.1088/0022-3727/28/11/012
[22] V.N. Ingal, E.A. Belyaevskaya. Tech. Phys., **42**, 59 (1997). DOI: 10.1134/1.1258639.
[23] M. Ando, R. Gupta, A. Iwakoshi, J.-K. Kim, D. Shimao, H. Sugiyama, N. Sunaguchi, T. Yuasa, S. Ichihara. Phys. Medica, **79** (3B), 188 (2020). DOI: 10.1016/j.ejmp.2020.11.034
[24] M. Ando, Y. Nakao, G. Jin, H. Sugiyama, N. Sunaguchi, Y. Sung, Y. Suzuki, Y. Sun, M. Tanimoto, K. Kawashima, T. Yuasa, K. Mori, S. Ichihara, R. Gupta. Med. Phys., **47** (11), 5505 (2020). DOI: 10.1002/mp.14442
[25] M. Ando, K. Hyodo, H. Sugiyama, A. Maksimenko, W. Pattanasiriwisawa, K. Mori, J. Roberson, E. Rubenstein, Y. Tanaka, J. Chen, D. Xian, X. Zhang. Jpn. J. Appl. Phys., **41** (7R), 4742 (2002). DOI: 10.1143/JJAP.41.4742
[26] M. Ando, H. Sugiyama, T. Kunisada, D. Shimao, K. Takeda, H. Hashizume, H. Inoue. Jpn. J. Appl. Phys., **43** (9AB), L1175 (2004). DOI: 10.1143/JJAP.43.L1175

[27] D. Shimao, H. Sugiyama, K. Hyodo, T. Kunisada, M. Ando. Nucl. Instrum. Methods A., **548** (1-2), 129 (2005). DOI: 10.1016/j.nima.2005.03.079
[28] D. Shimao, H. Sugiyama, T. Kunisada, M. Ando. Appl. Radiat. Isot., **64** (8), 868 (2006). DOI: 10.1016/j.apradiso.2006.03.004
[29] M. Ando, K. Yamasaki, F. Toyofuku, H. Sigiyama, C. Ohbayashi, G. Li, L. Pan, X. Jiang, W. Pattanasiriwisawa, D. Shimao, E. Hashimoto, T. Kimura, M. Tsuneyoshi, E. Ueno, K. Tokumori, A. Maksimenko, Y. Higashida, M. Hirano. Jpn. J. Appl. Phys., **44** (17), L528 (2005). DOI: 10.1143/JJAP.44.L528
[30] A. Snigirev, I. Snigireva, V. Kohn, S. Kuznetsov, I. Schelokov. Rev. Sci. Instrum., **66** (12), 5486 (1995). DOI: 10.1063/1.1146073
[31] S.W. Wilkins, T.E. Gureyev, D. Gao, A. Pogany, A.W. Stevenson. Nature, **384** (6607), 335 (1996). DOI: 10.1038/384335a0
[32] T.A. Leatham, D.M. Paganin, K.S. Morgan. arXiv:2112.10999v2 [physics.med-ph] (2022). DOI: 10.48550/arXiv.2112.10999
[33] M.R. Teague. J. Opt. Soc. Am., **73** (11), 1434 (1983). DOI: 10.1364/JOSA.73.001434
[34] P. Cloetens, W. Ludwig, J. Baruchel, D. Van Dyck, J. Van Landuyt, J.P. Guigay, M. Schlenker. Appl. Phys. Lett., **75** (19), 2912 (1999). DOI: 10.1063/1.125225
[35] D. Paganin, S.C. Mayo, T.E. Gureyev, P.R. Miller, S.W. Wilkins. J. Microsc., **206** (1), 33 (2002). DOI: 10.1046/j.1365-2818.2002.01010.x
[36] H. Risken. *The Fokker–Planck Equation: Methods of Solution and Applications*, 2nd edn (Springer Verlag, Berlin, 1989).
[37] Y.I. Nesterets. Opt. Commun., **281** (4), 533–542 (2008). DOI: 10.1016/j.optcom.2007.10.025
[38] D.M. Paganin, K.S. Morgan. Sci. Rep., **9** (1), 17537 (2019). DOI: 10.1038/s41598-019-52284-5
[39] J.N. Ahlers, K.M. Pavlov, M.J. Kitchen, K.S. Morgan. arXiv:2309.15874 (2023). DOI: 10.48550/arXiv.2309.15874
[40] A. Aminzadeh, B.D. Arhatari, A. Maksimenko, C.J. Hall, D. Hausermann, A.G. Peele, J. Fox, B. Kumar, Z. Prodanovic, M. Dimmock, D. Lockie, K.M. Pavlov, Y. I. Nesterets, D. Thompson, S.C. Mayo, D.M. Paganin, S.T. Taba, S. Lewis, P.C. Brennan, H.M. Quiney, T.E. Gureyev. IEEE Trans. Med. Imaging, **41** (11), 2980–2990 (2022). DOI: 10.1109/TMI.2022.3175924
[41] C. Gusenbauer, E. Leiss-Holzinger, S. Senck, K. Mathmann, J. Kastner, S. Hunger, W. Birkfellner. Case Stud. Nondestruct. Test. Eval., **6**, 30 (2016). DOI: 10.1016/j.csndt.2016.02.001
[42] S. Hu, L. Felsner, A. Maier, V. Ludwig, G. Anton, C. Riess. Sci. Rep., **9** (1), 9216 (2019). DOI: 10.1038/s41598-019-45708-9
[43] J. Graetz, A. Balles, R. Hanke, S. Zabler. Phys. Med. Biol., **65** (23), 235017 (2020). DOI: 10.1088/1361-6560/abb7c6
[44] H.F. Talbot. Phil. Mag., **9** (56), 401 (1836).
[45] A. Momose, S. Kawamoto, I. Koyama, Y. Hamaishi, K. Takai, Y. Suzuki. Jpn. J. Appl. Phys., **42** (7B), L866 (2003). DOI: 10.1143/JJAP.42.L866
[46] C. David, T. Weitkamp, F. Pfeiffer, A. Diaz, J. Bruder, T. Rohbeck, A. Groso, O. Bunk, M. Stampanoni, P. Cloetens. Proc. SPIE, **5535**, 137 (2004). DOI: 10.1117/12.569643
[47] T. Weitkamp, A. Diaz, C. David, F. Pfeiffer, M. Stampanoni, P. Cloetens, E. Ziegler. Opt. Express., **12** (16), 6296 (2005). DOI: 10.1364/OPEX.13.006296
[48] K. Scherer, E. Braig, K. Willer, M. Willner, A.A. Fingerle, M. Chabior, J. Herzen, M. Eiber, B. Haller, M. Straub, H. Schneider, E.J. Rummeny, P.B. Noël, F. Pfeiffer. Sci. Rep., **5** (1), 9527 (2015). DOI: 10.1038/srep09527
[49] M.P. Valdivia, D. Stutman, C. Stoeckl, C. Mileham, I.A. Begishev, J. Bromage, S.P. Regan. App. Opt., **57** (2), 138 (2018). DOI: 10.1364/AO.57.000138
[50] F. Pfeiffer, M. Bech, O. Bunk, T. Donath, B. Henrich, P. Kraft, C. David. J. Appl. Phys., **105** (10), 102006 (2009). DOI: 10.1063/1.3115639
[51] A. Momose, H. Takano, Y. Wu, K. Hashimoto, T. Samoto, M. Hoshino, Y. Seki, T. Shinohara. Quantum Beam Sci., **4** (1), 9 (2020). DOI: 10.3390/qubs4010009
[52] K. Li, Y. Ge, J. Garrett, N. Bevins, J. Zambelli. Med. Phys., **41** (1), 011903 (2014). DOI: 10.1118/1.4835455
[53] A. Yaroshenko, K. Hellbach, A.Ö. Yildirim, T.M. Conlon, F.I. Enlil, M. Bech, A. Velroyen, F.G. Meinel, S. Auweter, M. Reiser, O. Eickelberg, F. Pfeiffer. Sci. Rep., **5** (1), 17492 (2015). DOI: 10.1038/srep17492
[54] R. Burkhardt, T. Gora, A.A. Fingerle, A.P. Sauter, F. Meurer, F.T. Gassert, S. Dobiasch, D. Schilling, A. Feuchtinger, A.K. Walch, G. Multhoff, J. Herzen, P.B. Nöel, E.J. Rummeny, S.E. Combs, T.E. Schmid, F. Pfeiffer, J.J. Wilkens. Phys. Imaging Radiat. Oncol., **20**, 11 (2021). DOI: 10.1016/j.phro.2021.09.003
[55] M. Bech, A. Tapfer, A. Velroyen, A. Yaroshenko, B. Pauwels, J. Hostens, P. Bruyndonckx, A. Sasov, F. Pfeiffer. Sci. Rep., **3** (1), 3209 (2013). DOI: 10.1038/srep03209
[56] K. Hellbach, A. Yaroshenko, K. Willer, T. Pritzke, A. Baumann, N. Hesse, S. Auweter, M.F. Reiser, O. Eickelberg, F. Pfeiffer, A. Hilgendorff, F.G. Meinel. Invest. Radiol., **51** (10), 597 (2016). DOI: 10.1097/RLI.0000000000000285
[57] F.G. Meinel, A. Yaroshenko, K. Hellbach, M. Bech, M Müller., A. Velroyen, F. Bamberg, O. Eickelberg, K. Nikolaou, M.F. Reiser, F. Pfeiffer, A.Ö. Yildirim. Invest. Radiol., **49** (10), 653 (2014). DOI: 10.1097/RLI.0000000000000067
[58] K. Hellbach, F.G. Meinel, T.M. Conlon, K. Willer, A. Yaroshenko, A. Velroyen, M. Braunagel, S. Auweter, M.F. Reiser, O. Eickelberg, F. Pfeiffer, A.Ö. Yildirim. Sci. Rep., **8** (1), 2096 (2018). DOI: 10.1038/s41598-018-20193-8
[59] G.S. Zimmermann, A.A. Fingerle, B. Renger, K.-L. Laugwitz, H. Hautmann, A. Sauter, F. Meurer, F.T. Gassert, J. Bodden, C. Müller-Leisse, M. Renz, E.J. Rummeny, M.R. Makowski, K. Willer, W. Noichl, F. De Marco et al. Eur. Radiol. Exp., **6** (1), 9 (2022). DOI: 10.1186/s41747-022-00263-3
[60] H. Einarsdottir, M.J. Emerson, L.H. Clemmensen, K. Scherer, K. Willer, M. Bech, R. Larsen, B.K. Ersbøll, F. Pfeiffer. Food Control, **67**, 39 (2016). DOI: 10.1016/j.foodcont.2016.02.023
[61] E.M. Braig, L. Birnbacher, F. Schaff, L. Gromann, A. Fingerle, J. Herzen, E. Rummeny, P. Noël, F. Pfeiffer, D. Muenzel. Eur. Radiol. Exp., **2** (1), 1 (2018). DOI: 10.1186/s41747-017-0034-1
[62] H. Wen, E.E. Bennett, M.M. Hegedus, S. Rapacchi. Radiology, **251** (3), 910 (2009). DOI: 10.1148/radiol.2521081903

[63] C. Jud, E. Braig, M. Dierolf, E. Eggl, B. Günther, K. Achterhold, B. Gleich, E. Rummeny, P. Noël, F. Pfeiffer, D. Muenzel. Sci. Rep., **7** (1), 14477 (2017). DOI: 10.1038/s41598-017-14830-x
[64] N. Hauser, Z. Wang, R.A. Kubik-Huch, M. Trippel, G. Singer, Hohl, M.K. Roessl E., T. Köhler, U. van Stevendaal, N. Wieberneit, M. Stampanoni. Invest. Radiol., **49** (3), 131 (2014). DOI:10.1097/RLI.0000000000000001
[65] S. Grandl, K. Scherer, A. Sztrókay-Gaul, L. Birnbacher, K. Willer, M. Chabior, J. Herzen, D. Mayr, S.D. Auweter, F. Pfeiffer, F. Bamberg, K. Hellerhoff. Eur. Radiol., **25** (12), 3659 (2015). DOI:10.1007/s00330-015-3773-5
[66] K. Scherer, E. Braig, S. Ehn, J. Schock, J. Wolf, L. Birnbacher, M. Chabior, J. Herzen, D. Mayr, S. Grandl, A. Sztrókay-Gaul, K. Hellerhoff, F. Pfeiffer. Sci. Rep., **6** (1), 36991 (2016). DOI: 10.1038/srep36991
[67] S.H. Lau, S. Gull, G. Zan, D. Vine, S. Lewis, W. Yun. ISTFA Proceegings, Paper No: istfa2020p0079, 79–83 (2020). DOI: 10.31399/asm.cp.istfa2020p0079
[68] M. Bech, O. Bunk, T. Donath, R. Feidenhans'l, C. David, F. Pfeiffer. Phys. Med. Biol., **55** (18), 5529 (2010). DOI: 10.1088/0031-9155/55/18/017
[69] T. Lauridsen, E.M. Lauridsen, R. Feidenhans'l. Appl. Phys. A, **115** (3), 741 (2014). DOI: 10.1007/s00339-014-8398-z
[70] F. Schaff, F. Prade, Y. Sharma, M. Bech, F. Pfeiffer. Sci.Rep., **7** (1), 3307 (2017). DOI: 10.1038/s41598-017-03307-6
[71] T. Jensen, M. Bech, I. Zanette, T. Weitkamp, C. David, H. Deyhle, S. Rutishauser, E. Reznikova, J. Mohr, R. Feidenhans'l, F. Pfeiffer. Phys. Rev. B, **82** (21), 214103 (2010). DOI: 10.1103/PhysRevB.82.214103
[72] V. Revol, C. Kottler, R. Kaufmann, A. Neels, A. Dommann. J. Appl. Phys., **112** (11), 114903 (2012). DOI: 10.1063/1.4768525
[73] F.L. Bayer, S. Hu, A. Maier, T. Weber, G. Anton, T. Michel, C.P. Riess. Proc. Natl. Acad. Sci. USA., **111** (35), 12699 (2014). DOI: 10.1073/pnas.1321080111
[74] M. Wieczorek, F. Schaff, F. Pfeiffer, T. Lasser. Phys. Rev. Lett., **117** (15), 158101 (2016). DOI: 10.1103/PhysRevLett.117.158101
[75] A. Malecki, G. Potdevin, T. Biernath, E. Eggl, K. Willer, T. Lasser, J. Maisenbacher, J. Gibmeier, A. Wanner, F. Pfeiffer. PLoS ONE, **8** (4), e61268 (2013). DOI: 10.1371/journal.pone.0061268
[76] J. Vogel, F. Schaff, A. Fehringer, C. Jud, M. Wieczorek, F. Pfeiffer, T. Lasser. Opt. Express, **23** (12), 15134 (2015). DOI: 10.1364/OE.23.015134
[77] L. Felsner, S. Hu, A. Maier, J. Bopp, V. Ludwig, G. Anton, C. Riess. Sci. Rep., **9** (1), 9216 (2019). DOI: 10.1038/s41598-019-45708-9
[78] T. Zanette, T. Weitkamp, S. Donath, S. Rutishauser, C. David. Phys. Rev. Lett., **105** (24), 248102 (2010). DOI: 10.1103/PHYSREVLETT.105.248102
[79] C. Hannesschlägera, V. Revol, B. Plank, D. Salaberger, J. Kastnera. Case Stud. Nondestruct. Test Eval., **3**, 34 (2015). DOI: 10.1016/j.csndt.2015.04.001
[80] F. Prade, F. Schaff, S. Senck, P. Meyer, J. Mohr, J. Kastner, F. Pfeiffer. NDT E Int., **86** (7), 65 (2017). DOI: 10.1016/j.ndteint.2016.11.013
[81] J. Glinz, J. Šleichrt, D. Kytyr, S. Ayalur-Karunakaran, S. Zabler, J. Kastner, S. Senck. J. Mater. Sci., **56** (2), 9712 (2021). DOI: 10.1007/s10853-021-05907-0
[82] Y. Kasai, A. Yoshimura, M. Arai, K. Goto, A. Yamanaka, H. Shindo. Adv. Compos. Mater., **30** (6), 591–604 (2021). DOI: 10.1080/09243046.2021.1907877
[83] S. Reza, G. Pelzer, T. Weber, C. Fröjdh, F. Bayer, G. Anton, J. Rieger, J. Thim, T. Michel, B. Norlin. J. Instrumentation (JINST), **9** (04), C04032 (2014). DOI: 10.1088/1748-0221/9/04/C04032
[84] V. Ludwig, M. Seifert, T. Niepold, G. Pelzer, J. Rieger, J. Ziegler, T. Michel, G. Anton. J. Imaging, **4** (4), 58 (2018). DOI: 10.3390/jimaging4040058
[85] G. Potdevin, A. Malecki, T. Biernath, M. Bech, T.H. Jensen, R. Feidenhans'l, I. Zanette, T. Weitkamp, J. Kenntner, J. Mohr, P. Roschger, M. Kerschnitzki, W. Wagermaier, K. Klaushofer, P. Fratzl, F. Pfeiffer. Phys. Med. Biol., **57** (11), 3451 (2012). DOI: 10.1088/0031-9155/57/11/3451
[86] F. Schaff, A. Malecki, G. Potdevin, E. Eggl, P.B. Noël, T. Baum, E. Grande Garcia, J.S. Bauer, F. Pfeiffer. Sci. Rep., **4** (1), 3695 (2014). DOI: 10.1038/srep03695
[87] J. Scholz, N. Roiser, E.-M. Braig, C. Petrich, L. Birnbacher, J. Andrejewski, M.A. Kimm, A. Sauter, M. Busse, R. Korbel, J. Herzen, F. Pfeiffer. Sci. Rep., **11** (1), 19021 (2021). DOI: 10.1038/s41598-021-98151-0
[88] A. Olivo, F. Arfelli, G. Cantatore, R. Longo, R. H. Menk, S. Pani, M. Prest, P. Poropat, L. Rigon, G. Tromba, E. Vallazza, E. Castelli. Med. Phys., **28** (8), 1610 (2001). DOI: 10.1118/1.1388219
[89] A. Olivo, F. Arfelli, D. Dreossi, R. Longo, R.H. Menk, S. Pani, P. Poropat, L. Rigon, F. Zanconati, E. Castelli. Phys. Med. Biol., **47** (3), 469 (2002). DOI: 10.1088/0031-9155/47/3/308
[90] T.P. Millard, M. Endrizzi, K. Ignatyev, C.K. Hagen, P.R.T. Munro, R.D. Speller, A. Olivo. Rev. Sci. Instrum., **84** (8), 083702 (2013). DOI: 10.1063/1.4816827
[91] N. Matsunaga, K. Yano, M. Endrizzi, A. Olivo. J. Phys. D: Appl. Phys., **53** (9), 095401 (2020). DOI: 10.1088/1361-6463/ab5aa0
[92] M. Endrizzi, P. Diemoz, T. Millard, J.J. Louise, R. Speller, I. Robinson, A. Olivo. Appl. Phys. Lett., **104** (2), 024106 (2014). DOI: 10.1063/1.4861855
[93] M. Endrizzi, A. Olivo. J. Phys. D: Appl. Phys., **47** (50), 505102 (2014). DOI: 10.1088/0022-3727/47/50/505102
[94] E. Förster, K. Goetz, P. Zaumseil. Krist. Tech., **15** (8), 937 (1980). DOI: 10.1002/crat.19800150812
[95] V.A. Somenkov, A.K. Tkalich, S.S. Shil'shtein. Sov. Phys. Tech. Phys., **36**, 1309 (1991).
[96] T.J. Davis, D. Gao, T.E. Gureyev, A.W. Stevenson, S.W. Wilkins. Nature, **373** (6515), 595 (1995). DOI: 10.1038/373595a0
[97] V.A. Bushuev, V.N. Ingal, E.A. Belyaevskaya. Cryst. Rep., **41** (5), 766 (1996).
[98] D. Chapman, W. Thomlinson, R.E. Johnston, D. Washburn, E. Pisano, N. Gmür, Z. Zhong, R. Menk, F. Arfelli, D. Sayers. Phys. Med. Biol., **42** (11), 2015 (1997). DOI: 10.1088/0031-9155/42/11/001
[99] P. Suortti, J. Keyriläinen, W. Thomlinson. J. Phys. D: Appl. Phys., **46** (49), 494002 (2013). DOI: 10.1088/0022-3727/46/49/494002
[100] D.M. Connor, Z. Zhong. Curr. Radiol. Rep., **2** (7), 55 (2014). DOI: 10.1007/s40134-014-0055-y
[101] D. Mani, A. Kupsch, B.R. Müller, G. Bruno. J. Imaging, **8** (8), 206 (2022). DOI: 10.3390/jimaging8080206

[102] A. Bravin. J. Phys. D: Appl. Phys., **36** (10A), A24 (2003). DOI: 10.1088/0022-3727/36/10A/306
[103] P.C. Diemoz, P. Coan, C. Glaser, A. Bravin. Opt. Express., **18** (4), 3494 (2010). DOI: 10.1364/OE.18.003494
[104] L. Rigon, F. Arfelli, R. Menk. Appl. Phys. Lett., **90** (11), 114102 (2007). DOI: 10.1063/1.2713147
[105] L. Rigon, F. Arfelli, R.-H. Menk. J. Phys. D: Appl. Phys., **40** (10) 3077 (2007). DOI: 10.1088/0022-3727/40/10/011
[106] F. Arfelli, A. Astolfo, L. Rigon, R.H. Menk. Sci. Rep., **8** (1), 362 (2018). DOI: 10.1038/s41598-017-18367-x
[107] E. Pagot, P. Cloetens, S. Fiedler, A. Bravin, P. Coan, J. Baruchel, J. Härtwig, W. Thomlinson. Appl. Phys. Lett., **82** (20), 3421 (2003). DOI: 10.1063/1.1575508
[108] O. Oltulu, Z. Zhong, M. Hasnah, M.N. Wernick, D. Chapman. J. Phys. D: Appl. Phys., **36** (17), 2152 (2003). DOI: 10.1088/0022-3727/36/17/320
[109] M.N. Wernick, O. Wirjadi, D. Chapman, Z. Zhong, N.P. Galatsanos, Y. Yang, J.G. Brankov, O. Oltulu, M.A. Anastasio, C. Muehleman. Phys. Med. Biol., **48** (23), 3875 (2003). DOI: 10.1088/0031-9155/48/23/006
[110] M.J. Kitchen, D.M. Paganin, K. Uesugi, B.J. Allison, R.A. Lewis, S.B. Hooper, K.M. Pavlov. Opt. Express, **18** (19), 19994−20012 (2010). DOI: 10.1364/oe.18.019994
[111] M.J. Kitchen, D.M. Paganin, K. Uesugi, B.J. Allison, R.A. Lewis, S.B. Hooper, K.M. Pavlov. Phys. Med. Biol., **56** (3), 515−534 (2011). DOI: 10.1088/0031-9155/56/3/001
[112] M.J. Kitchen, G.A. Buckley, L.T. Kerr, K.L. Lee, K. Uesugi, N. Yagi, S.B. Hooper. Biomed. Opt. Express, **11** (8), 4176−4190 (2020). DOI: 10.1364/BOE.390587
[113] Ya.I. Nesterets, P. Coan, T.E. Gureyev, A. Bravin, P. Cloetens, S.W. Wilkins. Acta Crystallogr. A., **62** (Pt 4), 296 (2006). DOI: 10.1107/S0108767306017843
[114] H. Suhonen, M. Fernandez, A. Bravin, J. Keyrilainen, P. Suorttia. J. Synchrotron Rad., **14** (6), 512 (2007). DOI: 10.1107/S0909049507044664
[115] M. Fernández, H. Suhonen, J. Keyriläinen, A. Bravin, S. Fiedler, M.-L. Karjalainen-Lindsberg, M. Leidenius, K. von Smitten, P. Suortti. Eur. J. Radiol., **68** (3 Suppl), S89 (2008). DOI: 10.1016/j.ejrad.2008.04.039
[116] M. Giglio, M. Carpineti, A. Vailati. Phys. Rev. Lett., **85** (7), 1416 (2000). DOI: 10.1103/PhysRevLett.85.1416
[117] X. Lu, S.G.J. Mochrie, S. Narayanan, A.R. Sandy, M. Sprung. J. Synchrotron Rad., **18** (6), 823 (2011). DOI: 10.1107/S0909049511037149
[118] R. Cerbino, L. Peverini, M.A.C. Potenza, A. Robert, P. Bosecke, M. Giglio. Nature Phys., **4** (3), 238 (2008). DOI: 10.1038/nphys837
[119] S. Berujon, R. Cojocaru, P. Piault, R. Celestre, T. Roth, R. Barrett, E. Ziegler. J. Synchrotron Rad., **27** (2), 293 (2020). DOI: 10.1107/S1600577520000508
[120] I. Zanette, T. Zhou, A. Burvall, U. Lundström, D.H. Larsson, M. Zdora, P. Thibault, F. Pfeiffer, H.M. Hertz. Phys. Rev. Lett., **112** (25), 253903 (2014). DOI: 10.1103/PhysRevLett.112.253903
[121] M.-C. Zdora, P. Thibault, F. Pfeiffer, I. Zanette. J. Appl. Phys., **118** (11), 113105 (2015). DOI: 10.1063/1.4931145
[122] S. Bérujon, E. Ziegler, R. Cerbino, L. Peverini. Phys. Rev. Lett., **108** (15), 158102 (2012). DOI: 10.1103/PhysRevLett.108.158102
[123] K.S. Morgan, D.M. Paganin, K.K.W. Siu. Appl. Phys. Lett., **100** (12), 124102 (2012). DOI: 10.1063/1.3694918
[124] I.A. Aloisio, D.M. Paganin, C.A. Wright, K.S. Morgan. J. Synchrotron Rad., **22** (5), 1279-88 (2015). DOI: 10.1107/S1600577515011406
[125] S. Berujon, H. Wang, K. Sawhney. Phys. Rev. A, **86** (6), 063813 (2012). DOI: 10.1103/PhysRevA.86.063813
[126] M.-C. Zdora, P. Thibault, C. Rau, I. Zanette. J. Phys. Conf. Ser., **849** (1), 012024 (2017). DOI: 10.1088/1742-6596/849/1/012024
[127] H. Wang, Y. Kashyap, K. Sawhney. Appl. Phys. Lett., **108** (12), 124102 (2016). DOI: 10.1063/1.4944462
[128] S. Berujon, E. Ziegler. Phys. Rev. A, **92** (1), 013837 (2015). DOI: 10.1103/PhysRevA.92.013837
[129] S. Berujon, E. Ziegler. Phys. Rev. Applied, **5** (4), 044014 (2016). DOI: 10.1103/PhysRevApplied.5.044014
[130] R. Smith, F. De Marco, L. Broche, M.-C. Zdora, N.W. Phillips, R. Boardman, P. Thibault. PLoS ONE, **17** (8), e0273315 (2022). DOI: 10.1371/journal.pone.0273315
[131] K.M. Pavlov, D.M. Paganin, H. Li, S. Berujon, H. Rouge-Labriet, E. Brun. J. Opt., **22** (12), 125604 (2020). DOI: 10.1088/2040-8986/abc313
[132] K.M. Pavlov, D.M. Paganin, K.S. Morgan, H. (Thomas) Li, S. Berujon, L. Quénot, E. Brun. Phys. Rev. A, **104** (5), 053505 (2021). DOI: 10.1103/PhysRevA.104.053505
[133] D.M. Paganin, H. Labriet, E. Brun, S. Berujon. Phys. Rev. A, **98** (11), 053813 (2018). DOI: 10.1103/PhysRevA.98.053813
[134] K.M. Pavlov, H.T. Li, D.M. Paganin, S. Berujon, H. Rougé-Labriet, E. Brun. Phys. Rev. Appl., **13** (5), 054023 (2020). DOI: 10.1103/PhysRevApplied.13.054023
[135] S.J. Alloo, D.M. Paganin, K.S. Morgan, M.J. Kitchen, A.W. Stevenson, S.C. Mayo, H.T. Li, B.M. Kennedy, A. Maksimenko, J.C. Bowden, K.M. Pavlov. J. Med. Imaging, **9** (3), 031502 (2022). DOI: 10.1117/1.JMI.9.3.031502
[136] S.J. Alloo, K.S. Morgan, D.M. Paganin, K.M. Pavlov. Sci. Rep., **13** (1), 5424 (2023). DOI: 10.1038/s41598-023-31574-z
[137] C. Magnin, L. Quenot, S. Bohic, D.M. Cenda, M.F. Martínez, Bl. Lantz, B. Faure, E. Brun. arXiv:2304.10400 (2023).
[138] K.S. Morgan, D.M. Paganin, K.K. Siu. Opt. Express, **19** (20), 19781 (2011). DOI: 10.1364/OE.19.019781
[139] K.S. Morgan, P. Modregger, S.C. Irvine, S. Rutishauser, V.A. Guzenko, M. Stampanoni, C. David. Opt. Lett., **38** (22), 4605 (2013). DOI: 10.1364/OL.38.004605
[140] H. Wen, E.E. Bennett, M.M. Hegedus, S.C. Carroll. IEEE Trans. Med. Imaging, **27**(8), 997 (2008). DOI:10.1109/TMI.2007.912393
[141] Y.Y. How, K.S. Morgan. Opt. Express, **30** (7), 10899 (2022). DOI:10.1364/OE.451834
[142] Y.Y. How, D.M. Paganin, K.S. Morgan. Sci. Rep., **13** (1), 11001 (2023). DOI: 10.1038/s41598-023-37334-3
[143] S. Lang, I. Zanette, M. Dominietto, M. Langer, A. Rack, G. Schulz, G. Le Duc, C. David, J. Mohr, F. Pfeiffer, B. Müller, T. Weitkamp. J. Appl. Phys., **116** (15), 154903 (2014). DOI: 10.1063/1.4897225
[144] Y. Kashyap, H. Wang, K. Sawhney. Opt. Express, **24** (16), 18664 (2016). DOI: 10.1364/OE.24.018664
[145] J. Romell, T. Zhou, M. Zdora, S. Sala, F.J. Koch, H.M. Hertz, A. Burvall. J. Phys. Conf. Series, **849** (1), 012035 (2017). DOI: 10.1088/1742-6596/849/1/012035
[146] L. Quénot, S. Bohic, E. Brun. Appl. Sci., **12** (19), 9539 (2022). DOI: 10.3390/app12199539

[147] P. Modregger, Z. Wang, T. Thuering, B. Pinzer, M. Stampanoni. AIP Conf. Proc., **1365**, 269 (2011). DOI: 10.1063/1.3625356
[148] S. Kaeppler, J. Rieger, G. Pelzer, F. Horn, T. Michel, A. Maier, G. Anton, C. Riess. J. Med. Imag., **4** (3), 034005 (2017). DOI: 10.1117/1.JMI.4.3.034005
[149] J. Chen, J. Zhu, Z. Li, W. Shi, Q. Zhang, Z. Hu, H. Zheng, D. Liang, Y. Ge. Phys. Med. Biol., **64** (19), 195013 (2019). DOI: 10.1088/1361-6560/ab3c34
[150] C. Arboleda, Z. Wang, K. Jefimovs, T. Koehler, U. Van Stevendaal, N. Kuhn, B. David, S. Prevrhal, K. Lång, S. Forte, R.A. Kubik-Huch, C. Leo, G. Singer, M. Marcon, A. Boss, E. Roessl, M. Stampanoni. Eur. Radiol., **30** (2), 1419 (2020). DOI: 10.1007/s00330-019-06362-x
[151] A. Momose. Phys. Med., **79**, 93 (2020). DOI: 10.1016/j.ejmp.2020.11.003
[152] K. Willer, A.A. Fingerle, W. Noichl, F. De Marco, M. Frank, T. Urban, R. Schick, A. Gustschin, B. Gleich, J. Herzen, T. Koehler, A. Yaroshenko, T. Pralow, G.S. Zimmermann, B. Renger et al. Lancet Digit. Health., **3** (11), e733 (2021). DOI: 10.1016/S2589-7500(21)00146

Translated by D.Safin